Research Article Vol. 30, No. 3 / 31 Jan 2022 / Optics Express 3455
Optics EXPRESS

Computer-automated design of mode-locked fiber lasers

JAMES S. FEEHAN,[1,2,*] SAMUEL R. YOFFE,[1] ENRICO BRUNETTI,[1] MANUEL RYSER,[3,4] AND DINO A. JAROSZYNSKI[1]

[1]Scottish Universities Physics Alliance, Department of Physics, University of Strathclyde, Glasgow, G4 0NG, UK
[2]Currently with Fraunhofer Centre for Applied Photonics, 99 George Street, Glasgow, G1 1RD, UK
[3]Institute of Applied Physics, University of Bern, Sidlerstrasse 5, 3012 Bern, Switzerland
[4]8photonics GmbH, Lorystrasse 6, 3008 Bern, Switzerland
*james.feehan@fraunhofer.co.uk

Abstract: We automate the mode-locked fiber laser design process using a modified genetic algorithm and an intuitive optimization loss function to control highly accurate polarization-resolved simulations of laser start-up dynamics without user interaction. We reconstruct both the cavity designs and output pulse characteristics of experimentally demonstrated Yb-fiber all-normal dispersion, dispersion-managed, and wavelength-tuneable all-anomalous dispersion Tm-fiber femtosecond lasers with exceptional accuracy using minimal prior knowledge, and show that our method can be used to predict new cavity designs and novel mode locking states that meet target pulse requirements. Our approach is directly applicable to a broad range of mode locking regimes, wavelengths, pulse energies, and repetition rates, requires no training or knowledge of the loss function gradients, and is scalable for use on supercomputers and inexpensive desktop computers.

Published by Optica Publishing Group under the terms of the Creative Commons Attribution 4.0 License. Further distribution of this work must maintain attribution to the author(s) and the published article's title, journal citation, and DOI.

1. Introduction

Owing to their low cost, compactness, environmental stability, and diffraction-limited beam quality, mode-locked fiber lasers have had a substantial impact on many fields of research including medicine and the life sciences, materials processing, metrology, and frequency conversion [1–7]. Growing demand for new wavelength regimes, higher repetition rates and greater pulse peak powers continues to drive the discovery of new lasers and mode locking states. Despite significant progress over the past two decades [8–16], finding and engineering new designs that meet application requirements remains a considerable challenge.

In-depth knowledge of the highly nonlinear intracavity field evolution during both start-up and steady-state operation is a crucial requirement for tackling this problem. Modern measurement techniques provide invaluable insights [17,18], but a quantitative analysis of intracavity dynamics is difficult to achieve using experiments alone. Numerical models have therefore become essential [8–10,14]. However, there is a tradeoff between model precision and ease of implementation because the design parameter space increases to an unmanageable size as simplifying approximations are removed, so manual parameter searches become infeasible as models become more sophisticated. A reliable method for achieving a precise, quantitative match between simulations and experiments that resolves this tradeoff would greatly accelerate research and allow mode-locked fiber laser design to be fully automated and tailored to application requirements if combined with an appropriate optimization algorithm.

Interest in integrating machine learning with ultrafast optics is increasing rapidly [19], and so far attention has largely been focused on automated control of experiments using evolutionary

#450059 https://doi.org/10.1364/OE.450059
Journal © 2022 Received 30 Nov 2021; revised 5 Jan 2022; accepted 7 Jan 2022; published 18 Jan 2022

Optics EXPRESS

algorithms for enhanced performance and functionality [20–23], and rapid prediction of the outcome of nonlinear dynamics simulations using, for example, long short-term memory (LSTM) neural networks [24]. Particle swarm optimization (PSO) has also been demonstrated as an effective method for finding mode locking states in a simulation of a figure-of-eight fiber laser [25], but the underlying model relied on a simplified description of gain, was restricted to second-order dispersion and self-phase modulation only, and no comparison with experiments was made. Therefore, to the best of our knowledge, no method for overcoming the precision/implementation tradeoff has been proposed.

In this work, we use a modified genetic algorithm (GA) to achieve exceptional precision in numerical simulations of experimentally demonstrated ultrafast fiber lasers and their output pulses reliably with minimal prior knowledge and user input, thereby solving the tradeoff and demonstrating computer-automated design of mode-locked fiber lasers for the first time. A highly accurate polarization-resolved numerical model based on the generalized nonlinear Schrödinger equation (GNLSE) is controlled by the GA, which optimizes simulation parameters such as pump power, fiber lengths, intracavity dispersion management, and polarization control. We use the combined model and GA to fully reconstruct laser designs and output pulse characteristics from three previously reported experiments covering a range of mode locking regimes: an all-normal dispersion Yb-fiber laser [10], a gigahertz (GHz) dispersion-managed Yb-fiber laser [11], and a Tm-fiber soliton laser exhibiting broad wavelength tunability from 1867 – 2010 nm [12]. Our approach is intuitive and requires no prior knowledge of the search space, optimization function gradients, or training.

We achieve an excellent quantitative match between simulations and experiments by excluding many common simplifying approximations and including comprehensive models of gain, bulk and fiber-based components, the full wavelength-dependent fiber dispersion profiles and effective mode areas, and quantum noise contributions at all lossy interfaces *e.g.*, fiber splice points. The laser performance characteristics retrieved by the GA agree almost exactly with experiments, and the retrieved design parameters have an average error of 4%. This far exceeds the accuracy that we were able to achieve from the same model by manually searching the design parameter space. Additionally, autocorrelations of compressed output pulses, pulse durations, energies, spectra, repetition rates, and other characteristics such as wavelength tunability are all reconstructed with very high accuracy. We show that our method is reliable and capable of predicting cavity designs that meet target pulse parameters, is suitable for quantitative laser performance analyses specific to individual laser builds and experiments, is appropriate for the automated discovery of exotic mode locking regimes (such as multi-pulse states), and that it can modify existing cavity designs to alter output pulse characteristics selectively, which is particularly challenging to do using experiments alone.

Our method is directly applicable to the design of novel fiber lasers such as mid-infrared cavities based on soft-glass fibers for surgical applications and ultrafast molecular fingerprinting [13,26–29], as well as the exploration of novel mode locking states that are challenging to observe in both experiments and simulations, such as those exhibited by ultrafast multi-wavelength lasers [14] and Raman-based sources of noise-like pulses [30]. Our technique will benefit the development of other devices that can be modelled accurately using the GNLSE, such as those based on supercontinuum generation as well as fiber amplifier and chirped-pulse amplification systems. With the inclusion of multiple transverse modes in our propagation model, future development could target free-space and multimode systems for beam combination, alignment, and wavefront management in high-energy systems [31], novel techniques such as spatiotemporal mode locking [32], and automated waveguide design for applications in, *e.g.*, pulse self-compression and high-harmonic generation [33–35].

The genetic algorithm and numerical model are summarized in section 2. The computer-automated mode-locked fiber laser design technique is demonstrated and verified against

Optics EXPRESS

experimental laser systems in section 3. Section 4 contains a discussion on the broader application of our approach and potential improvements, and the work is concluded in section 5.

2. Genetic algorithm and numerical model

We define the population of laser parameters as a matrix with designs ('individuals') stored in the rows and design parameters ('genes'), such as pump power and pump wavelength, stored in the columns. Mutation, crossover, and selection operations are applied to the population to randomly generate new genes, produce new individuals by combining the genes of two others, and to rank individuals based on whether their genes result in a stable simulation output which matches a target power spectral density (PSD) and reptition rate. This match is quantified using the optimization loss, η, given in Eq. (1). η is calculated for all individuals in the population, and the best-fit individual returns the smallest value (*i.e.*, the GA minimizes η).

$$\eta = (1 + |\Delta f|/f_t)^N \int_{\lambda_{min}}^{\lambda_{max}} \left[|\tilde{T}(\lambda) - \tilde{S}(\lambda)| + \sum_{i=n-9}^{n} |\tilde{S}_i(\lambda) - \tilde{S}_{i-1}(\lambda)| \right] d\lambda \tag{1}$$

Δf is the difference between the simulated repetition rate and the target repetition rate, f_t, and n is the total number of round trips. $\tilde{T}$ is the target output PSD, $\tilde{S}$ is the simulated output PSD after the final round trip, and λ is wavelength. The term including $|\tilde{T} - \tilde{S}|$ ensures that η is proportional to the difference between the target and simulated spectra. The other terms in the integrand are the sum of the absolute differences between the simulated output PSDs over the final 10 round trips, and ensure that η increases with round-trip spectral instability. We found that 10 round trips was adequate for allowing the GA to assess stability, and the summation was used instead of, for example, the relative intensity noise or first-order degree of coherence [36,37] because it is faster to compute and has the same units as the first term. Multiplying by $(1 + |\Delta f|/f_t)^N$ encourages solutions with repetition rates close to f_t, constraining the cavity length. $N \geq 0$ was used to control the importance of this constraint relative to the match between target and simulated PSDs and the shot-to-shot stability terms. Although the repetition rate contribution would be negated if both integrands evaluate to zero (giving $\eta = 0$ W and leading to a false optimization), in practice, quantum noise contributions and minor differences between simulated and experimental fiber and component parameters mitigate this outcome.

The target PSD, $\tilde{T}(\lambda)$, can be defined numerically (*e.g.*, using a Gaussian or parabola) or appropriately scaled experimental data can be used. Using a numerically-defined target allows for cavity design without prior experimentation, but in this work we use scaled experimental data to test that our computer-automated design approach is reliable by accurately recreating real cavities and their optical performance. We then demonstrate how this method can be used to predict new cavity designs to meet target laser requirements.

We restrict the population size to 60 individuals to verify that our approach is appropriate for affordable workstation computers. Small populations negatively impact genetic diversity, which requires careful management for rapid convergence and a thorough exploration of the search space, so we included in our GA an elitism algorithm [38] that we modified to include 'challenger' solutions. Respectively, these additions allow the best-fit (elite) individuals to pass directly from one generation to the next and create new (challenger) individuals whose genes are selected from narrow normal distributions with mean values equal to the elite genes. Elitism prevents best-fit solutions from being lost to mutation and crossover operations, which encourage search space exploration. Including challengers encourages search space exploitation.

The number of elites, challengers and how often they are introduced, the mutation rate, and N must be selected carefully for the GA to converge quickly. We chose to keep three elite solutions after a trial and error approach, and found that three challenger solutions introduced once for every five consecutive generations without a reduction in η was adequate. The convergence

Optics EXPRESS

rate had no strong dependence on the crossover point, so this was set to $\lfloor n_{\text{genes}}/2 \rfloor$ (n_{genes} is the number of genes in an individual). Non-local exploration was very important, so the mutation probability was given a high value of 5%. N was selected on a case-by-case basis and typically had a value of 1 or 2.

The mode-locked laser simulations controlled by the GA were based on the full polarization-resolved generalized nonlinear Schrödinger equation (GNLSE). Our model included measured fiber loss [39], dispersion, birefringence, self-phase modulation, self steepening, cross-phase modulation, polarization-based instabilities and modulation instability, degenerate four-wave mixing between polarization components and relevant phasematching conditions, as well as the full polarization-dependent Raman response [40,41]. Gain was simulated using a comprehensive frequency-domain model and measured emission and absorption cross sections [42,43].

Fiber dispersion profiles and propagation parameters such as the mode field diameter were calculated as a function of wavelength using the method outlined in Refs. [44,45] and the manufacturers' documentation. Component and fiber birefringence information was obtained from manufacturers' documentation or, if unavailable, was left as a free parameter to be optimized by the GA. Polarization effects were incorporated in full using Jones calculus [46], which allowed for accurate definitions of bulk and fiber-coupled components with the inclusion of wavelength-dependent loss, quantum noise contributions [47], and estimations of polarization crosstalk due to axis misalignment. Loss due to Fresnel reflections was included at all component interfaces as well as wavelength-dependent losses at splices and free-space to fiber coupling points [48]. See appendices A and B for further details regarding the model and simulation starting conditions. See appendix C for a summary of all fibers used in the simulations.

3. Automated mode-locked fiber laser design

Fig. 1 shows the three exemplar laser designs that we use to verify our computer-automated design approach. Lasers A, B, and C are Yb-fiber all-normal dispersion (ANDi), Yb-fiber dispersion-managed, and Tm-fiber wavelength-tunable soliton lasers, respectively, and are discussed in detail in Refs. [10–12]. These designs cover a diverse set of mode locking types due to their different formats (all-fiber and fiber/free-space hybrid), rare-earth dopants, intracavity dispersion (all-normal, managed, and all-anomalous), repetition rates, and pulse characteristics. We focus on nonlinear polarization evolution (NPE) mode locking [49] because the polarization coupling of the spectral and temporal pulse shaping results in complex and rich cavity dynamics that can be very difficult to reproduce numerically using manual parameter selection [19]. (Our approach is not limited to NPE, and with minor adaptation to the underlying model could include, *e.g.*, Fabry-Perot cavities [50] and nonlinear amplifying loop mirrors [51] for optimizing cavity designs with improved environmental stability [52], see Appendix A). Consequently, our selection of laser designs is suitable for testing our computer-automated design algorithm comprehensively.

In the following, we discuss the performance of the computer-automated design algorithm for each laser in turn, beginning with the ANDi laser from Ref. [10] (design A, Fig. 1). Reconstructions of all three laser designs and their output pulses are optimized using the output spectra from each laser design as the target in Eq. (1). Comparisons between reconstructed and experimental parameters from Refs. [10–12] are given in this section, and a full summary of reconstructed parameters is given in Appendix D.

For the ANDi laser, the waveplate angles, Yb-fiber pump absorption per unit length, fiber group velocity mismatch (GVM), the four HI1060 lengths and the Yb-fiber length were left as free parameters for the GA to optimize. It was possible to fully reconstruct the laser design and performance by setting only the bandpass filter transmission width, the pump wavelength and power delivered to the gain fiber as constants, and these were equal to 10 nm, 976 nm, and 350 mW, respectively, as per Ref. [10]. Additionally, we set $N = 1$ in Eq. (1). The HI1060 and

Optics EXPRESS

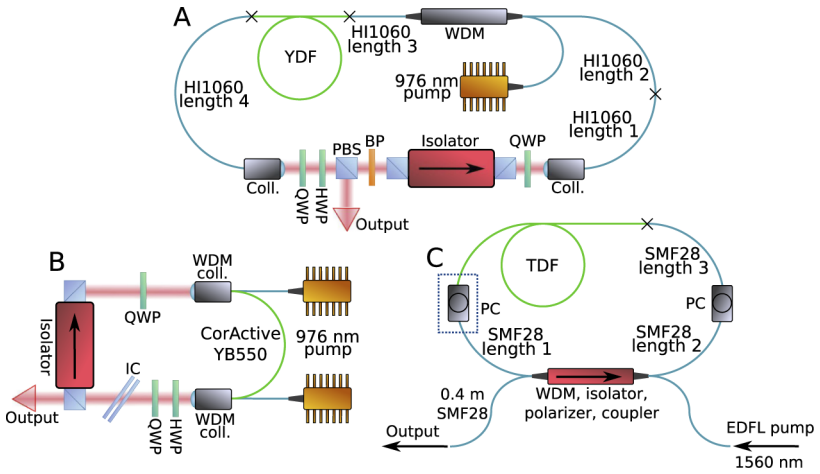

Fig. 1. Schematics of the laser designs reconstructed by the GA. A: All-normal dispersion Yb-fiber laser [10]. B: 1 GHz dispersion-managed Yb-fiber laser [11]. C: Soliton Tm-fiber laser with wavelength tuning from 1867–2010 nm [12]. QWP and HWP: quarter- and half-wave plate, respectively. PBS: polarizing beam splitter. BP: Bandpass filter. Coll.: collimator. WDM: wavelength division multiplexer. WDM coll.: collimator with integrated WDM. IC: intracavity compressor. TDF: thulium-doped fiber. EDFL: erbium-doped fiber laser. PC: polarization controller. Crosses denote splice points.

Yb-fiber lengths used in the experiment are given in this reference, so a direct comparison can be made with the reconstructed laser design.

The optimization loss, η, is shown as a function of generation number in Fig. 2(A). Further optimization would be incremental, so the GA was terminated after 500 generations with a final loss value of 20.5 mW (optimization time of 13 hours, single laser simulation time of 25 seconds). The simulated and experimentally measured PSDs match closely (Fig. 2(B)), and the reconstructed and target pulse energies are 2.8 nJ and 2.7 nJ, respectively. Furthermore, the time-domain characteristics of the simulated laser design are in excellent agreement with the experiment even though they are not targeted directly by the GA. Firstly, the simulated pulses are compressible, as shown by Fig. 2(C) which compares the transform limit of the experimentally measured ANDi laser output (TL, gray) with the simulated output pulse after a grating-based compressor simulation has been applied (comp., green, see Appendix A for details of the pulse compression). The peak power of the compressed pulse is 87% of the experimental transform limited value, and its chirp, λ (red dashed curve), is flat over the central peak. Secondly, the reconstructed compressed pulse full width at half maximum (FWHM) duration of 150 fs compares favorably with the 170 fs duration inferred from autocorrelation measurements in Ref. [10]. The experimental and simulated autocorrelations (Fig. 2(D)) and the FWHM duration of the pulses before compression match closely (3.3 ps and 3 ps for the simulations and experiments, respectively). The simulated chirp is positive and predominantly linear throughout the cavity as expected for this laser design, and the excellent match between the simulations and experiments of the spectral and temporal performance characteristics indicates that the intracavity field evolution is retrieved with high accuracy.

The cavity fiber lengths and repetition rate are also retrieved with very high accuracy, confirming that the GA can retrieve both the laser design and its performance when only the bandpass and pump parameters are known. The average error between the retrieved fiber lengths and those reported in Ref. [10] is 5% (see Table 1). The reconstructed and target repetition rates are 44 MHz and 45 MHz, respectively. A close match between the simulated and experimental laser

Optics EXPRESS

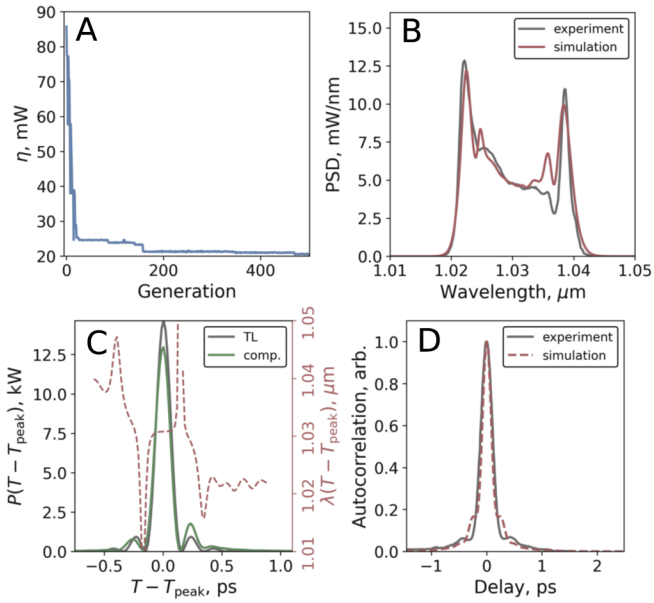

Fig. 2. Reconstruction of the ANDi Yb-fiber laser (design A, Fig. 1). A: η as a function of generation number. B: Experimentally measured and simulated spectra. C: Transform limit calculated from the experimentally measured spectrum (TL), and the simulated compressed output pulse (comp.) and chirp. D: Comparison between the simulated and measured autocorrelations of the compressed pulses. The measured spectrum and measured autocorrelation were digitized from [10]. Visualization 1 shows the full ANDi laser reconstruction.

performance was also found after just 25 generations, where η falls to 25 mW, but the fiber lengths for this solution have a $\sim$ 20% error.

Table 1. Comparison of the fiber lengths for the experimentally demonstrated and reconstructed ANDi lasers (design A, Fig. 1; Ref. [10])

Fiber	Experiment	Reconstruction	% error
HI1060 1+2+3	3 m	3.1 m	3.3
HI1060 4	1 m	1.03 m	3
Yb-fiber	0.2 m	0.18 m	10

The same reconstruction quality is also retrieved for the 1 GHz dispersion-managed Yb-fiber laser reported by Li, *et al.* [11] (design B, Fig. 1). Only the pump power and pump wavelength were fixed for this reconstruction (set to 1.8 W and 976 nm, respectively, matching the experiment). The free parameters were the Yb-doped fiber length and pump absorption per unit length, the fiber GVM, wave plate angles, and the compressor incident angle and grating separation. We attribute the need for fewer fixed parameters to the high repetition rate, which simplifies the design to a single fiber and provides a harder constraint on the acceptable range of fiber lengths. Initially, we used $N = 1$ in Eq. (1), but this weighted the match to the target PSD too strongly in comparison with the repetition rate and the GA could not retrieve the experimental cavity parameters, so the optimization was conducted a second time using $N = 2$.

The loss for the reconstruction using $N = 2$ is shown as a function of generation number in Fig. 3(A), and the final value is 87 mW (optimization time of 2 hours, single laser simulation

Optics EXPRESS

time of 7 seconds). The output PSD of the reconstructed laser is an excellent match with the experimental data, as shown by Fig. 3(B), and an 80 dB pulse contrast over the full time window confirms that mode locking was observed in the simulations. The output pulse characteristics of the reconstructed laser (Fig. 3(C)) match the experimentally measured values very closely, with compressed FWHM durations of 62 fs and 63 fs, respectively, and transform limited FWHM durations of 60 fs for both [11].

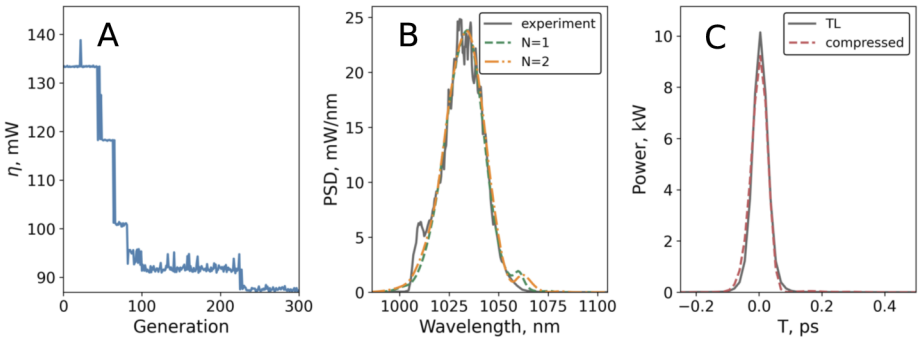

Fig. 3. Reconstruction of the 1 GHz Yb-fiber laser (design B, Fig. 1). A: η as a function of generation number. B: Experimentally measured and simulated spectra using $N = 1$ and 2 in Eq. (1). C: Transform limit and compressed pulses using $N = 2$. The measured spectrum was digitized from [11].

Both values of N resulted in final optimization loss values of ~ 87 mW and the corresponding reconstructed PSDs are an equally good match to the experiment. Similarly, the output average powers match the experimental value of 600 mW closely, with values of 594 mW and 618 mW for $N = 1$ and 2, respectively. However, the fiber length, intracavity compressor dispersion, repetition rate and, consequently, the pulse energy do not match the experimental values when $N = 1$.

Both the excellent accuracy of the laser reconstruction when $N = 2$ and the poor cavity design parameter retrieval when $N = 1$ are summarized in Table 2. The average error between the reconstructed and experimental parameters is 2.4% for the former and 18% for the latter. $N = 2$ results in a better match between the repetition rates of the reconstructed and experimental lasers, as expected, and this in turn improves the match for the Yb-fiber length and the intracavity compressor dispersion. We note that although correctly weighting the PSD and repetition rate contributions in Eq. (1) is a considerable challenge for computer-automated mode-locked laser design, it can also be achieved with $N = 1$ if fewer free design parameters are used during the optimization by including measured component properties in the simulations (*e.g.*, transmission profiles and beat lengths).

Table 2. Comparison of key laser parameters for the experimentally demonstrated and reconstructed GHz lasers (design B, Fig. 1; Ref. [11]). f_r: repetition rate. IC β_2: intracavity compressor second-order dispersion.

parameter	Experiment	Reconstruction		% error	
		$N = 1$	$N = 2$	$N = 1$	$N = 2$
f_r	1 GHz	0.91 GHz	1.03 GHz	9	3
Yb-fiber	0.13 m	0.15 m	0.125 m	15.4	3.8
IC β_2	-5000 fs^2	-6467 fs^2	-4976 fs^2	29.3	0.5

Optics EXPRESS

To retrieve the Tm-fiber laser design and performance reported by Sun *et al.* [12] (design C, Fig. 1), we first reconstructed the laser using a target spectrum centered at 1940 nm (the middle of the tuning range). The Tm-fiber and SMF-28 lengths, polarization control, and fiber group velocity were left as free parameters, and $N = 1$. The pump power could vary between 340 – 600 mW, where single-pulse mode locking was reported, and the only fixed parameters were the pump wavelength (1560 nm) and absorption of the Tm-fiber (65 dB/m, approximating that of commercial Tm-fibers). A single fiber-based polarization controller was used for wavelength tuning via Lyot filtering in the experiments [12], and this was incorporated in our model using Jones matrices for a quarter-wave plate between SMF-28 2 and 3 in design C, Fig. 1 and for quarter- and half-wave plates between the Tm-fiber and SMF-28 1 (dotted rectangle).

The reconstruction quality of the Tm-fiber laser is summarized in Table 3. The fiber lengths are retrieved with an average error of 3.6% and the repetition rates match to within 1%. In experiments, self-starting mode locking was reported for a pump power of 575 mW and could be maintained for pump powers above 380 mW [12]. This was not observed in our reconstruction, and we attribute this to an inaccurate estimation of the pump insertion loss of the hybrid WDM, isolator, polarizer, and coupler component. However, the retrieved pump power of 350 mW is close to the lower experimental value. Both the target and reconstructed PSDs exhibit soliton characteristics (Fig. 4(A)) and the final loss value for this optimization was 22.5 mW after 300 generations (optimization time of 7 hours, single laser simulation time of 22 seconds).

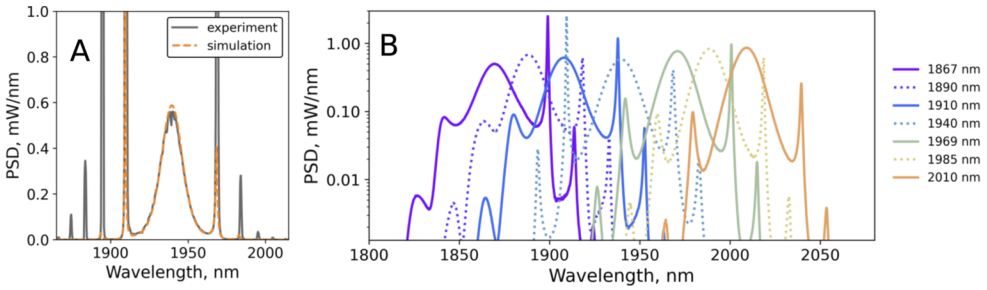

Fig. 4. Reconstruction of the femtosecond Tm-doped fiber laser with polarization-based wavelength tuning (design C, Fig. 1). A: Output spectra measured from experiments and from the reconstructed laser design at 1940 nm (measured spectrum digitized from [12]). B: Simulated output spectra for different polarization controller settings, showing that the experimentally demonstrated wavelength tuning range of 1867 – 2010 nm was retrieved by the GA.

Table 3. Comparison of key parameters for the experimentally demonstrated and reconstructed wavelength-tunable Tm-fiber lasers (design C, Fig. 1; Ref. [12])

Parameter	Experiment	Reconstruction	% error
SMF-28 1+2+3	0.4 m	0.42 m	5
Tm-fiber	0.4 m	0.38 m	5
Pump power	575 mW, 380 mW	350 mW	39, 8
f_r	248 MHz	246 MHz	0.8

The reconstructed laser performance matches the experiments closely over the full tuning range detailed in Ref. [12], and the simulated polarization-based wavelength tuning retrieved by the GA is shown in Fig. 4(B). The wavelength tunability was retrieved by using each spectrum in Ref. [12] as a target and re-optimizing the cavity polarization control (all other parameters were

Optics EXPRESS

held constant, mirroring the experiments). Additionally, to prevent the wavelength variation of the fiber effective index from modifying η through minor changes to the repetition rate, we set $N = 0$ and replaced the PSD with the energy spectral density in Eq. (1) when reconstructing the wavelength tunability.

For all reconstructions, the simulated PSDs and Kelly sideband wavelengths are close to an exact match with the experiments, indicating accurate reproduction of the cavity Lyot filtering and dispersion. The energy in the Kelly sidebands is not reproduced, and this may be due to the pump power mismatch, or because their association with reduced pulse stability means their development is suppressed by the stability terms in Eq. (1) [53]. However, neglecting the Kelly sidebands, the average error in output pulse energy is $\sim 3\%$ between the experimental and reconstructed lasers. The pulse durations after a 40 cm length of OFS-980 at the laser output were ~ 380 fs in the experiments and are ~ 400 fs in the simulations, respectively [12], further confirming the excellent reconstruction accuracy over the full wavelength tuning range.

4. Discussion

We have shown that the mode-locked fiber laser design process can be automated given a suitable target spectrum and repetition rate. Here, we discuss the broader application of our approach and outline some potential improvements.

Our GA-based optimization increases the size of the manageable search space in comparison with manual parameter selection, allowing for simplifying approximations to be removed and an excellent quantitative match between simulations and experiments. For example, we make no assumptions about the frequency-domain gain shape or values for small-signal and saturable gain, fiber dispersion, or which nonlinear effects are negligible. Additionally, because the NPE is modelled in full, we also make no assumptions about the effect of the saturable absorber on the peak intensity, spectrum, chirp, or polarization state. Our approach therefore allows accurate analyses of mode-locked laser performance where manually selecting design parameters would be too time consuming for a detailed model to be beneficial.

The combination of the GA and detailed cavity model thereby results in simulations that are accurate enough to be applied to specific laser units. This is of great interest in industrial environments, allowing for laser design tolerances, specifications, and causes of quality control issues with, *e.g.*, central wavelength, bandwidth, and pulse compressibility to be found numerically, complementing an experimental approach by reducing manufacturing time and cost. Furthermore, preliminary testing has shown that LSTM neural networks are a promising route for fast and optimization-free automated laser design when trained using simulation data produced by the GA during optimization. LSTM has also been applied to other nonlinear optical systems [24,54,55] and, together with computer-automated design and recent progress in the use of machine learning algorithms in experiments [20–22], could be used as an alternative to population-based optimization algorithms for rapid self-tuning and stabilization of 'smart' lasers and for computer-assisted diagnosis of laser system performance issues.

Our approach can also be used for automated discovery if suitable modifications are made to the loss function (Eq. (1)), as was demonstrated when reconstructing the wavelength tunability of the Tm-fiber laser. As a further example, Figs. 5(A) and 5(B) show the onset of a stable multi-pulse mode locking state found by the GA during the ANDi laser optimization discussed in section 3. Solutions such as this are often difficult to find but yield useful information regarding the intracavity dynamics. Specifically, three key features of the onset of multi-pulse mode locking are shown. Firstly, the wavelength-domain plot (Fig. 5(A)) shows that the second pulse is generated from an instability in the first (round trips 20 – 40). Secondly, both of the pulse peaks advance along the time axis by the same amount each round trip (-50 fs, Fig. 5(B)), indicating that both have the same polarization state with a dominant fast-axis field component. Thirdly, the damped, out-of-phase relaxation oscillations between the pulses indicate a strong initial

Optics EXPRESS

competition for stored energy (round trips 45 to 120). During the optimization, the GA exchanged this solution for one that matches the target parameters more closely. However, mode locking states such as this can be targeted by including terms in Eq. (1) that favour, for example, multiple peaks in the time domain or spectral modulations, allowing the GA to find stable multi-pulse, multi-wavelength, and other exotic mode locking states for target applications.

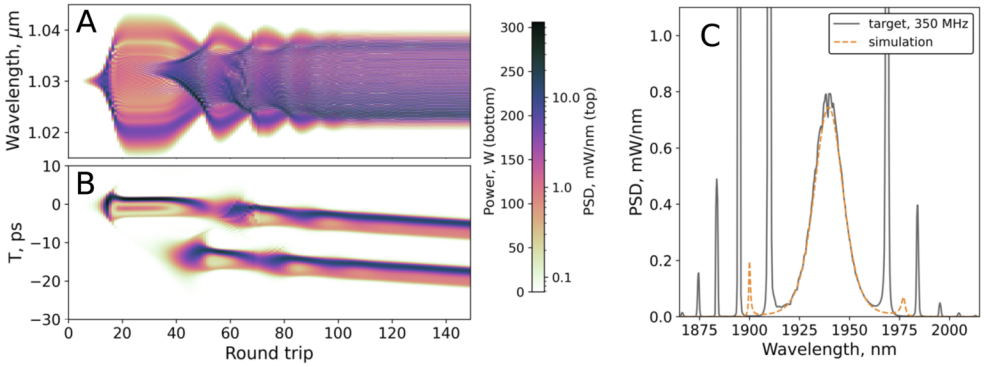

Fig. 5. A and B: ANDi Yb-fiber laser output during the onset of stable multi-pulse mode locking, shown in the wavelength and time domains, respectively (design A, Fig. 1). This is an intermediate solution found by the GA during the reconstruction discussed in section 3. C: Output of a Tm-doped fiber laser designed by the GA, based on design C, Fig. 1 and targeting the same power spectral density at a higher repetition rate of 350 MHz.

Our approach is also effective at finding design modifications that change performance characteristics selectively. This is particularly challenging to do in experiments. To demonstrate this, we used our GA to predict which parameters of the 1940 nm Tm-fiber laser (design C, Fig. 1) must be changed to increase the repetition rate from 248 MHz to 350 MHz while keeping the PSD the same. The Tm-fiber pump absorption per unit length was the same as that used in section 3, but all other parameters were freely adjustable. Figure 5(C) shows the target spectrum and the simulated PSD, and the predicted laser design parameters are given in Table 4. There is little change in the active fiber lengths between the 248 MHz and 350 MHz cavity designs, but the total amount of passive fiber is reduced by approximately 40% from 0.42 m to 0.25 m (see Table 3). The pump power remains approximately the same and the output coupling, which was freely adjustable using the polarization control, halves from 14% for the 248 MHz cavity to 7% for the 350 MHz cavity. These changes are realistic; keeping the PSDs the same causes the average power to remain the same and so the same pump power is required, but increasing the repetition rate reduces the pulse energy and hence the required second-order dispersion to maintain the soliton pulse shape. The wider spacing of the Kelly sidebands for 350 MHz is due to the shorter round trip (perturbation) period of this cavity design.

Table 4. Predicted cavity parameters for a 350 MHz Tm-doped fiber laser based on design C, Fig. 1; Ref. [12].

SMF-28	Tm-fiber	Pump power	f_r
0.25 m	0.31 m	355 mW	350 MHz

By using the 248 MHz laser design as a starting point, the 350 MHz design was optimized in approximately 45 minutes using a consumer-grade CPU (AMD Ryzen 3950x). For the full laser reconstructions in section 3, an optimized laser design was typically reached in under 15 hours. Significant effort was made to minimize execution time of the laser simulations (Appendix E)

Optics EXPRESS

so any further reduction in convergence time is most likely to be found in the way we manage genetic diversity. A simple approach would be to increase the population size and available computing power, but this is often inefficient and expensive. Instead, a promising route is the dynamic control of both the number of challengers and the variance with which their genes are selected based on the generation number, population genetic diversity, and convergence rate. This approach is, in principle, similar to simulated annealing, which in future research could also be included alongside the elitism and challengers algorithms to encourage non-local exploration in the early stages of the optimization.

5. Conclusion

We have introduced a modified genetic algorithm as an effective and efficient route for the automated design of mode-locked fiber lasers, precise numerical experimentation, and for analyses of cavity dynamics that are directly applicable to specific laser builds and experiments. This was achieved by using the GA to optimize the input parameters of a highly accurate numerical model that is too detailed for manual parameter selection to be effective because of the size of the parameter space. We verified our technique by reconstructing experimentally demonstrated all-normal dispersion, dispersion managed, and soliton mode-locked fiber laser designs with excellent accuracy, retrieving both performance and cavity design for all three laser types with minimal prior knowledge, including: the output power spectral density, pulse energy, average power, and repetition rate; key cavity parameters such as intracavity compressor dispersion, fiber lengths, and pump power; and notable performance characteristics such as output pulse compressibility, pulse duration, and polarization-based wavelength tunability. Additionally, we have shown that our technique is applicable to different wavelength regimes and active dopants as long as fiber propagation loss and transition cross sections are known.

By incorporating elitism and challengers algorithms into our GA, we maintained a good balance between search space exploration and exploitation on affordable, consumer-grade hardware while retaining scalability for use on national high-performance computing facilities. We presented a loss function that ensures convergence towards targeted laser performance and is suitable for many optimization algorithms including, for example, PSO [25]. Potential improvements to our approach were discussed, such as the inclusion of simulated annealing and dynamic adjustment of the challengers algorithm to reduce convergence time. Our computer-automated design technique is immediately applicable to the development of novel ultrafast mid-infrared sources [13,26–29], and can be applied to the development of fiber amplifier systems, supercontinuum sources, and other nonlinear optical devices.

Appendix A. Mode-locked fiber laser simulations

The mode-locked laser simulations were based on the generalized nonlinear Schrödinger equation (GNLSE), defined as

$$\frac{\partial A(z,T)}{\partial z} = \left[\hat{L} + \hat{N}\right] A(z,T). \tag{2}$$

The complex field envelope was defined using a linear polarization basis $A(z,T) = \hat{x}A_x(z,T) + \hat{y}A_y(z,T)$, where $\hat{x}$ and $\hat{y}$ are orthogonal unit vectors. $\hat{L}$ and $\hat{N}$ are linear and nonlinear operators, discussed below. T is the retarded time frame given by $T = t - z/\Delta\nu_g$, where $\Delta\nu_g = \nu_{gx} - \nu_{gy}$ is the difference in group velocity between the polarization modes.

Solutions to Eq. (2) were found using the integration and adaptive step sizing methods outlined in Refs. [57] and [58], respectively. The polarization dependence of each operator was included using Jones calculus [46] because it has been shown previously that this provides an accurate and easily implemented route for simulating polarization dynamics of nonlinear fiber systems using the GNLSE and a linear polarization basis [14,59,60].

Optics EXPRESS

$$\hat{L}(\Omega) = \frac{\alpha(\Omega)}{2} - i\left[\Delta\beta_1\Omega - \frac{\beta_2(\Omega)}{2}\Omega^2\right] \tag{3}$$

The linear operator, $\hat{L}(\Omega)$ (Eq. (3)), included the full fiber dispersion profile ($\beta_2(\Omega)$), loss ($\alpha(\Omega)$), and the polarization GVM ($\Delta\beta_1$). $\Omega = \omega - \omega_0$ is the angular frequency grid centered at 0 THz. β_2 included both the material and waveguide contributions and their wavelength dependence, and was calculated for each fiber using the Sellmeier equations and the method in Ref. [44]. We made no assumptions about the influence of higher-order dispersion terms or the choice of fiber type, and dispersion profiles were included in full (see Fig. 6 for an example dispersion profile calculated using this method and specifications for SMF-28 which matches published values of 18 ps/(nm km) and 22 ps/(nm km) at 1550 nm and 1625 nm, respectively [61]). The polarization group velocity mismatch (GVM, $\Delta\beta_1$) was calculated for each fiber using published birefringence information where available. If no birefringence information was found, the GVM was left as a free parameter to be optimized by the GA. We adopted the convention that $\Delta\beta_{1x} = (\beta_{1x} - \beta_{1y})/2$ and $\Delta\beta_{1y} = (\beta_{1y} - \beta_{1x})/2$, resulting in A_x and A_y moving in opposite directions relative to $T = 0$ ps at group velocities with magnitude $\Delta\beta_1/2$. Fiber loss was equal to that of standard single-mode silica fibers (Fig. 6, digitized from [39]).

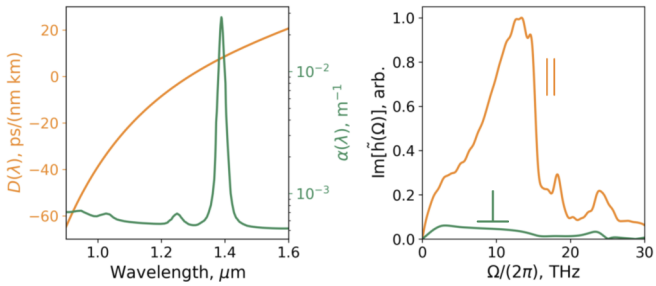

Fig. 6. Left: Single-mode fiber loss (green, right axis) and example dispersion based on SMF-28 (orange, left axis). Right: Raman gain spectra for co- and cross-polarized light (|| and ⊥, respectively).

The nonlinear operator, $\hat{N}$, was defined using Eq. (4) (z and T dependence omitted for brevity and $k, l = x, y : k \neq l$), and accounted for self-steepening, self-phase modulation, cross-phase modulation, and degenerate four-wave mixing (DFWM, terms in $A_k^\star A_l$ and $A_k A_l^\star$) between polarization components for both the instantaneous and delayed (Raman) nonlinear response. We have included the DFWM phasematching dependence on the fiber birefringence, $\Delta n = |n_x - n_y|$, and the phasematching argument is negative for $k = x$. The $*$ symbol denotes convolution. The strength of the nonlinear response is governed by $\gamma = 2\pi n_2/(\lambda A_{\text{eff}}(\lambda))$, where n_2 is the nonlinear index, λ is wavelength, and A_{eff} is the effective mode field area. A_{eff} and hence γ were calculated as a function of wavelength using the mode field diameter (MFD) and information given in the publications detailing the laser designs and the documentation published by the fiber manufacturers alongside the method in Ref. [45]. Calculated MFDs were in excellent agreement with the documentation.

$$\begin{aligned}\hat{N}_k A_k = -i\gamma\left(1 + \frac{1}{\omega_0}\frac{\partial}{\partial T}\right)\Bigg[(1 - f_R)\left(|A_k|^2 A_k + \frac{2}{3}|A_l|^2 A_k + \frac{1}{3}A_k^\star A_l^2 e^{\pm 4\pi i \Delta n z/\lambda}\right) \\ + f_R\left(A_k(a+b) * |A_k|^2 + A_k a * |A_l|^2 + A_l\frac{b}{2} * \left(A_k A_l^\star + A_l A_k^\star e^{\pm 4\pi i \Delta n z/\lambda}\right)\right)\Bigg]\end{aligned} \tag{4}$$

Optics EXPRESS

The full polarization-resolved Raman response was included through parameters a and b, which were calculated using the method outlined in Ref. [41] using the fused silica Raman response functions for co- and orthogonally-polarized signals digitized from Ref. [40]. The resulting Raman gain spectra for co- and cross-polarized signals are shown in the right-hand plot of Fig. 6. With the inclusion of the co- and cross-polarized Raman contributions, parametric mixing and phasematching, birefringence, and phase modulation terms, Eqs. (3) and 4 account for all relevant linear and nonlinear polarization effects.

Gain and absorption of the signal and pump light in the doped fibers were calculated as a function of wavelength using the measured emission and absorption cross sections shown in Fig. 7. We assumed only co-propagating signals were significant to reduced code execution time, which is justified because an isolator was used in each laser considered. By removing this assumption, our model could be adapted for co- and counter-propagating signals (required for Fabry-Perot cavities [50] and nonlinear amplifying loop mirrors [51], for example).

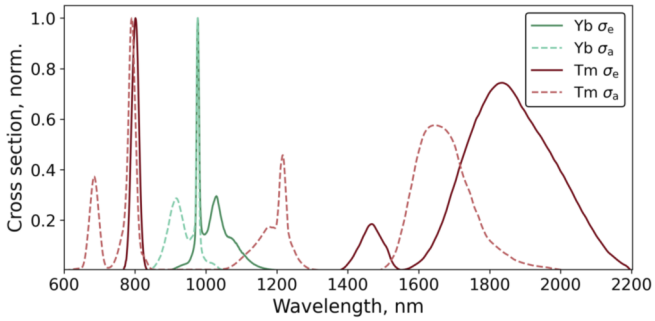

Fig. 7. Emission and absorption cross sections used in the simulations (normalized). The Tm-fiber cross sections were digitized from Ref. [43].

We assumed that only frequency-domain gain effects were significant, and this was verified by testing cavity designs both with and without the effects of gain-phase modulation [62]. Incorporating time-domain gain effects also resulted in an additional overhead which made our simulations too slow for effective optimization. We also found that our implementation of gain-phase modulation reduced the accuracy of the spectral gain shape, which was important for modeling its effect on quantum noise contributions.

Optical components were defined using Jones matrices for polarization control including retardation, beam splitting, extinction, and the spectral transmission data such as bandwidth and loss. This data was measured from components with the same specifications as those detailed in Refs. [10–12] or estimated from component documentation. Wavelength-dependent loss due to Fresnel reflections at interfaces between air and fiber or free-space components was also estimated using calculated refractive index data and assuming normal incidence, permitted because of the small incidence angles of free-space optics and small cleave angles at free-space to fiber couplings in typical cavities. Wavelength-dependent loss at fiber splices was calculated using the method in Ref. [48]. Estimations of polarization crosstalk due to imperfect axis alignment were also included for each component. All sources of loss included a quantum noise contribution calculated using the wavelength-dependent loss and photon spectrum [47].

The dispersion profiles of the grating-based pulse compressors was modeled up to the fifth order and was controlled by specifying the grating separation and angle of incidence [63]. Diffraction efficiency was included using a scalar approach [64] which approximated the dependence on wavelength, blaze, and angle of incidence. The intracavity compressor used in the 1 GHz Yb-fiber laser model [11] was based on specifications for commercial transmission gratings. All other grating-based compressor simulations included in their loss profile the reflectivity of

Optics EXPRESS

gold as a function of wavelength. Compression of the simulated output pulses was done using the grating-based compressor model or by simulating linear propagation in single-mode fiber, depending on which method was used by the authors of the works on which our laser models are based. Optimum parameters for compressing the output pulses (*i.e.*, the grating separation and incident angle or the fiber length) were found using the Nelder-Mead algorithm [65] with basin hopping to minimize the absolute difference between the peak powers of the compressed pulse and the transform limit.

Appendix B. Simulation starting conditions, time-frequency grid definition, and repetition rate calculations

One photon per mode quantum noise was used as the starting field for both polarization basis vectors, A_x and A_y. This is a common method for including quantum noise in simulations of nonlinear polarization dynamics based on the GNLSE [59,60,66]. Initial testing showed that the onset of mode locking was highly probabilistic, as expected, and could take hundreds of round trips or tens of thousands depending on the input quantum noise. This made it very difficult to define stop criteria for the laser design optimization, so we added a 1 fJ, 1 ps Gaussian starting pulse to the quantum noise field to stabilize the number of round trips required for mode locking to <150. We saw no change to the mode locked solutions for starting pulse energies between 50 aJ and 20 fJ, or for different starting pulse shapes (including sech^2, super-Gaussian up to order 10, and Lorentzian).

The simulation time-frequency grid had 2^{11} points and a time span of 34 ps for the Yb-fiber lasers and 60 ps for the Tm-fiber laser. The repetition rate of the all-fiber Tm laser was calculated using $f_\text{r} = 1/\tau$, where τ is the round trip time calculated using the group velocities [44] and lengths of the cavity fibers. To calculate the repetition rate of the simulated Yb-fiber lasers, the propagation time of the free-space cavity sections in the experimental lasers was required. First, the round trip time of the experimental laser was retrieved using $\tau = 1/f_\text{r}$. Then, the time spent propagating in the cavity fibers in the experiment, τ_fiber, was retrieved using the published cavity fiber lengths and calculated group velocities, and the free-space propagation time was calculated using $\tau_\text{free} = \tau - \tau_\text{fiber}$. The simulated round trip time was then calculated for each laser design in the population using $\tau_\text{sim} = \tau_\text{free} + \tau_\text{fiber sim}$, where $\tau_\text{fiber sim}$ was calculated using the group velocities and lengths of the simulated cavity fibers. The repetition rates of the simulated lasers were retrieved using $f_\text{r sim} = 1/\tau_\text{sim}$.

Appendix C. Summary of fiber properties

Table 5 summarizes key parameters of the passive and active fibers used in the simulations. Unless otherwise specified, the HI1060 and Yb-fiber parameters are given for 1030 nm, SMF-28 parameters for 1550 nm, and Tm-fiber parameters for 1940 nm. The dispersion is truncated to second order for brevity, but the full dispersion curve was used in the simulations.

The geometrical fiber parameters were based closely on manufacturers' design specifications. If no product name or manufacturer was given in the original publication (as was the case for the Tm-doped fiber used in Ref. [12]), we chose fiber parameters that resulted in a close match to the given dispersion, NA, and effective mode field area. Our values for some of the geometric parameters (*e.g.*, core diameter, NA) deviate slightly from manufacturers' design specifications so that our models closely matched the derived parameters (*e.g.*, effective mode area, dispersion) with those given in Refs. [10–12] and the manufacturers' documentation. Our chosen values for the geometric parameters are within specified manufacturing tolerances.

Optics EXPRESS

Table 5. Summary of the fiber parameters used in the simulations. Core ⊘: core diameter. dn: refractive index step. NA: numerical aperture. MFD: mode field diameter. D: dispersion parameter.

Manufacturer	Fiber name	Core ⊘(μm)	dn($\times 10^{-3}$)	NA	MFD (μm)	D(ps/(nm km))
Corning	HI 1060	5.6	6.7	0.14	6.1(1.06 μm)	-41.5
Corning	SMF-28	8.2	5	0.12	10.2 (12.6,1.94 μm)	17.9 (38.5,1.94 μm)
–	YDF	4	13.7	0.2	4.3	-43.8
CorActive	SCF-YB550-4/125-19	4	12.4	0.19	4.4	-46.4
–	TDF	4.4	25.1	0.27	5.6	16

Appendix D. Summary of reconstructed laser parameters

Parameters for the final optimized designs of the ANDi, GHz Yb-fiber, and tunable Tm-fiber lasers are given in Tables 6, 7, and 8, respectively. HWP and QWP: half- and quarter-wave plate, respectively. GVM: Group velocity mismatch. IC: Intracavity compressor. PC: polarization control. For the Tm-fiber laser, PC angles are for Jones matrices equivalent to half- and two quarter-wave plates. Error values for the retrieved parameters are given where a comparison could be drawn with experimental values. We have indicated in the error column where the parameter was fixed, no experimental data was given (*e.g.*, polarization control), or where specifications for component parameters were not reported (*e.g.*, the active fiber pump absorption per unit length).

Table 6. All-normal dispersion Yb-fiber laser parameters.

Parameter	Value	% error
HI 1060 1 + 2 + 3	3.1 m	3.3
HI 1060 4	1.03 m	3
Yb-fiber	0.18 m	10
Pump absorption (976 nm)	1000 dB/m	not reported
Pump power	350 mW	fixed
Pump wavelength	976 ± 0.5 nm	fixed
GVM (beat length)	-3.47 fs/m (0.98 m)	not reported
HWP, QWP, QWP angles	2.12, -0.97, -2.39 rad	not reported

Table 7. Dispersion-managed 1 GHz Yb-fiber laser parameters.

Parameter	Value	% error
Yb-fiber	0.125 m	3
Pump absorption (976 nm)	900 dB/m	not reported
Pump power	1.8 W	fixed
Pump wavelength	976 ± 0.5 nm	fixed
GVM (beat length)	1.43 fs/m (2.4 m)	not reported
HWP, QWP, QWP angles	0.99, 0.61, -0.39 rad	not reported
IC (separation, angle)	0.65 mm, 25°	0.5 (β_2)

Optics EXPRESS

Table 8. Wavelength-tunable Tm-fiber laser parameters.

Parameter	Value	% error
SMF-28 1+2+3	0.42 m	5
Tm-fiber	0.38 m	5
Pump absorption (1560 nm)	65 dB/m	not reported
Pump power	350 mW	8
Pump wavelength	1560 ± 0.5 nm	fixed
PC angles	1.79, -0.82, -2.4 rad	not reported
GVM (beat length)	-4.06 fs/m (1.59 m)	not reported

Appendix E. Hardware and execution time

Our laser simulation software was designed to be 'perfectly parallel' in order to reduce the time required to test all lasers in each generation. Recent studies of nonlinear fiber systems have used general-purpose graphics processing units to run simulations in parallel (GPGPU, *e.g.* Refs. [59,60,67]), but we found that the requirement to batch operations made it difficult to stabilize the integration error when using adaptive step sizing because of the different intracavity peak intensities of each laser design in a generation. This resulted in a stochastic simulation output, preventing convergence towards a single laser design.

We used CPU-based parallel computing to mitigate this issue by distributing each laser simulation as its own process. Benefits of this approach are twofold: it allows the adaptive step sizing algorithm to stabilize the integration error of each test cavity independently and, unlike GPGPUs, high-throughput double-precision mathematics required for the simulations is not restricted to high-end CPUs. Our software therefore scales for use on any computer, ranging from national high-performance computing facilities to affordable workstations as the laser design complexity and size of the search space requires.

This choice of hardware along with a thorough optimization of our code allowed the GA to converge quickly. Typically, each generation of 60 individuals took on the order of one minute to complete on a consumer-grade CPU (AMD Ryzen 9 3950x) but, in general, the execution time is inversely proportional to the repetition rate of the laser. For example, the Yb-fiber dispersion-managed 1 GHz oscillator [11] required <30 s for each generation, whereas the Yb-fiber ANDi 45 MHz oscillator [10] took approximately 3 minutes. A full laser optimization took between 1 and 24 hours with our hardware, but this convergence rate could be improved by up to a factor of four by using a newer CPU with more physical cores.

Funding. Engineering and Physical Sciences Research Council (EP/N028694/1).

Acknowledgements. J. Feehan, S. Yoffe, E. Brunetti and D. Jaroszynski thank Dr. Annalisa Riccardi (University of Strathclyde) for helpful suggestions regarding the GA. J. Feehan is grateful to Dr. Jonathan Price (University of Southampton) for providing the Yb-fiber spectroscopy data. Very sadly, Jonathan passed away before we had the opportunity to discuss this work.

Disclosures. The authors declare no conflicts of interest.

Data availability. Data underlying the results presented in this paper are available in Ref. [56].

References

1. C. H. Tischbirek, T. Noda, M. Tohmi, A. Birkner, I. Nelken, and A. Konnerth, "In vivo functional mapping of a cortical column at single-neuron resolution," Cell Rep. **27**(5), 1319–1326.e5 (2019).
2. F. Morin, F. Druon, M. Hanna, and P. Georges, "Microjoule femtosecond fiber laser at 1.6 μm for corneal surgery applications," Opt. Lett. **34**(13), 1991–1993 (2009).
3. Y. Jung, A. Kennedy, H. Chiu, F. Mohammad, A. Claridge-Chang, and D. J. Anderson, "Neurons that function within an integrator to promote a persistent behavioral state in drosophila," Neuron **105**(2), 322–333.e5 (2020).

Optics EXPRESS

4. B. Öktem, I. Pavlov, S. Ilday, H. Kalaycıoğlu, A. Rybak, S. Yavaş, M. Erdoğan, and F. Ö. Ilday, "Nonlinear laser lithography for indefinitely large-area nanostructuring with femtosecond pulses," Nat. Photonics **7**(11), 897–901 (2013).
5. L. Shah, A. Y. Arai, S. M. Eaton, and P. R. Herman, "Waveguide writing in fused silica with a femtosecond fiber laser at 522 nm and 1 MHz repetition rate," Opt. Express **13**(6), 1999–2006 (2005).
6. S. Okubo, A. Onae, K. Nakamura, T. Udem, and H. Inaba, "Offset-free optical frequency comb self-referencing with an f-2f interferometer," Optica **5**(2), 188–192 (2018).
7. T. O. Buchmann, E. J. R. Kelleher, M. Jazbinsek, B. Zhou, J.-H. Seok, O.-P. Kwon, F. Rotermund, and P. U. Jepsen, "High-power few-cycle THz generation at MHz repetition rates in an organic crystal," APL Photonics **5**(10), 106103 (2020).
8. B. Oktem, C. Ülgüdür, and F. Ö. Ilday, "Soliton-similariton fibre laser," Nat. Photonics **4**(5), 307–311 (2010).
9. N. Davoudzadeh, G. Ducourthial, and B. Q. Spring, "Custom fabrication and mode-locked operation of a femtosecond fiber laser for multiphoton microscopy," Sci. Rep. **9**(1), 4233 (2019).
10. A. Chong, J. Buckley, W. Renninger, and F. Wise, "All-normal-dispersion femtosecond fiber laser," Opt. Express **14**(21), 10095–10100 (2006).
11. C. Li, Y. Ma, X. Gao, F. Niu, T. Jiang, A. Wang, and Z. Zhang, "1 GHz repetition rate femtosecond Yb:fiber laser for direct generation of carrier-envelope offset frequency," Appl. Opt. **54**(28), 8350–8353 (2015).
12. B. Sun, J. Luo, Z. Yan, K. Liu, J. Ji, Y. Zhang, Q. J. Wang, and X. Yu, "1867-2010 nm tunable femtosecond thulium-doped all-fiber laser," Opt. Express **25**(8), 8997–9002 (2017).
13. S. D. Jackson, "Towards high-power mid-infrared emission from a fibre laser," Nat. Photonics **6**(7), 423–431 (2012).
14. J. S. Feehan, F. Ö. Ilday, W. S. Brocklesby, and J. H. V. Price, "Simulations and experiments showing the origin of multiwavelength mode locking in femtosecond, Yb-fiber lasers," J. Opt. Soc. Am. B **33**(8), 1668–1676 (2016).
15. F. Wise, A. Chong, and W. Renninger, "High-energy femtosecond fiber lasers based on pulse propagation at normal dispersion," Laser & Photon. Rev. **2**(1-2), 58–73 (2008).
16. N. Bawden, O. Henderson-Sapir, S. D. Jackson, and D. J. Ottaway, "Ultrafast 3.5 μm fiber laser," Opt. Lett. **46**(7), 1636–1639 (2021).
17. J. Peng, M. Sorokina, S. Sugavanam, N. Tarasov, D. V. Churkin, S. K. Turitsyn, and H. Zeng, "Real-time observation of dissipative soliton formation in nonlinear polarization rotation mode-locked fibre lasers," Commun. Phys. **1**(1), 20 (2018).
18. G. Herink, B. Jalali, C. Ropers, and D. R. Solli, "Resolving the build-up of femtosecond mode-locking with single-shot spectroscopy at 90 MHz frame rate," Nat. Photonics **10**(5), 321–326 (2016).
19. G. Genty, L. Salmela, J. M. Dudley, D. Brunner, A. Kokhanovskiy, S. Kobtsev, and S. K. Turitsyn, "Machine learning and applications in ultrafast photonics," Nat. Photonics **15**(2), 91–101 (2021).
20. G. Pu, L. Yi, L. Zhang, and W. Hu, "Intelligent programmable mode-locked fiber laser with a human-like algorithm," Optica **6**(3), 362–369 (2019).
21. R. I. Woodward and E. J. R. Kelleher, "Towards 'smart lasers': self-optimisation of an ultrafast pulse source using a genetic algorithm," Sci. Rep. **6**(1), 37616 (2016).
22. S. Mahmoodi, C. Bacher, A. Heidt, C. Lätt, D. Abdollahpour, V. Romano, T. Feurer, and M. Ryser, "Ultrashort pulse formation from a thulium-doped fiber laser: Self-characterization and mapping," Opt. Commun. **486**, 126747 (2021).
23. L. Michaeli and A. Bahabad, "Genetic algorithm driven spectral shaping of supercontinuum radiation in a photonic crystal fiber," J. Opt. **20**(5), 055501 (2018).
24. L. Salmela, N. Tsipinakis, A. Foi, C. Billet, J. M. Dudley, and G. Genty, "Predicting ultrafast nonlinear dynamics in fibre optics with a recurrent neural network," Nat Mach Intell **3**(4), 344–354 (2021).
25. A. Kokhanovskiy, E. Kuprikov, A. Bednyakova, I. Popkov, S. Smirnov, and S. Turitsyn, "Inverse design of mode-locked fiber laser by particle swarm optimization algorithm," Sci. Rep. **11**(1), 13555 (2021).
26. T. Hu, S. D. Jackson, and D. D. Hudson, "Ultrafast pulses from a mid-infrared fiber laser," Opt. Lett. **40**(18), 4226–4228 (2015).
27. M. R. Majewski, R. I. Woodward, and S. D. Jackson, "Ultrafast mid-infrared fiber laser mode-locked using frequency-shifted feedback," Opt. Lett. **44**(7), 1698–1701 (2019).
28. S. Antipov, D. D. Hudson, A. Fuerbach, and S. D. Jackson, "High-power mid-infrared femtosecond fiber laser in the water vapor transmission window," Optica **3**(12), 1373–1376 (2016).
29. S. A. Diddams, L. Hollberg, and V. Mbele, "Molecular fingerprinting with the resolved modes of a femtosecond laser frequency comb," Nature **445**(7128), 627–630 (2007).
30. D. Li, D. Shen, L. Li, H. Chen, D. Tang, and L. Zhao, "Raman-scattering-assistant broadband noise-like pulse generation in all-normal-dispersion fiber lasers," Opt. Express **23**(20), 25889–25895 (2015).
31. D. Wang and Y. Leng, "Simulating a four-channel coherent beam combination system for femtosecond multi-petawatt lasers," Opt. Express **27**(25), 36137–36153 (2019).
32. L. G. Wright, D. N. Christodoulides, and F. Wise, "Spatiotemporal mode-locking in multimode fiber lasers," Science **358**(6359), 94–97 (2017).
33. J. Travers, T. Grigorova, C. Brahms, and F. Belli, "High-energy pulse self-compression and ultraviolet generation through soliton dynamics in hollow capillary fibres," Nat. Photonics **13**(8), 547–554 (2019).
34. P. N. Anderson, P. Horak, J. G. Frey, and W. S. Brocklesby, "High-energy laser-pulse self-compression in short gas-filled fibers," Phys. Rev. A **89**(1), 013819 (2014).

Optics EXPRESS

35. B. Dromey, M. Zepf, M. Landreman, and S. Hooker, "Quasi-phasematching of harmonic generation via multimode beating in waveguides," Opt. Express **15**(13), 7894–7900 (2007).
36. K. L. Corwin, N. R. Newbury, J. M. Dudley, S. Coen, S. A. Diddams, B. R. Washburn, K. Weber, and R. S. Windeler, "Fundamental amplitude noise limitations to supercontinuum spectra generated in a microstructured fiber," Appl. Phys. B **77**(2-3), 269–277 (2003).
37. J. M. Dudley and S. Coen, "Coherence properties of supercontinuum spectra generated in photonic crystal and tapered optical fibers," Opt. Lett. **27**(13), 1180–1182 (2002).
38. S. Baluja and R. Caruana, "Removing the genetics from the standard genetic algorithm," in *Machine Learning Proceedings 1995*, A. Prieditis and S. Russell, eds. (Morgan Kaufmann, 1995), pp. 38–46.
39. T. Miya, Y. Terunuma, T. Hosaka, and T. Miyashita, "Ultimate low-loss single-mode fibre at 1.55 μm," Electron. Lett. **15**(4), 106–108 (1979).
40. R. H. Stolen, J. P. Gordon, W. J. Tomlinson, and H. A. Haus, "Raman response function of silica-core fibers," J. Opt. Soc. Am. B **6**(6), 1159–1166 (1989).
41. S. Trillo and S. Wabnitz, "Parametric and Raman amplification in birefringent fibers," J. Opt. Soc. Am. B **9**(7), 1061–1082 (1992).
42. R. Paschotta, J. Nilsson, A. Tropper, and D. Hanna, "Ytterbium-doped fiber amplifiers," IEEE J. Quantum Electron. **33**(7), 1049–1056 (1997).
43. D. Creeden, B. R. Johnson, G. A. Rines, and S. D. Setzler, "High power resonant pumping of Tm-doped fiber amplifiers in core- and cladding-pumped configurations," Opt. Express **22**(23), 29067–29080 (2014).
44. D. Gloge, "Weakly guiding fibers," Appl. Opt. **10**(10), 2252–2258 (1971).
45. C. D. Hussey and F. Martinez, "Approximate analytic forms for the propagation characteristics of single-mode optical fibres," Electron. Lett. **21**(23), 1103–1104 (1985).
46. R. C. Jones, "A new calculus for the treatment of optical systems I. Description and discussion of the calculus," J. Opt. Soc. Am. **31**(7), 488–493 (1941).
47. B. Huttner and Y. Ben-Aryeh, "Influence of a beam splitter on photon statistics," Phys. Rev. A **38**(1), 204–211 (1988).
48. D. Marcuse, "Loss analysis of single-mode fiber splices," The Bell Syst. Tech. J. **56**(5), 703–718 (1977).
49. K. Tamura, H. A. Haus, and E. P. Ippen, "Self-starting additive pulse mode-locked erbium fiber ring laser," Electron. Lett. **28**(24), 2226–2228 (1992).
50. L. Lefort, J. H. V. Price, D. J. Richardson, G. J. Spühler, R. Paschotta, U. Keller, A. R. Fry, and J. Weston, "Practical low-noise stretched-pulse Yb^{3+}-doped fiber laser," Opt. Lett. **27**(5), 291–293 (2002).
51. M. E. Fermann, F. Haberl, M. Hofer, and H. Hochreiter, "Nonlinear amplifying loop mirror," Opt. Lett. **15**(13), 752–754 (1990).
52. W. Hänsel, H. Hoogland, M. Giunta, S. Schmid, T. Steinmetz, R. Doubek, P. Mayer, S. Dobner, C. Cleff, M. Fischer, and R. Holzwarth, "All polarization-maintaining fiber laser architecture for robust femtosecond pulse generation," Appl. Phys. B **123**(1), 41 (2017).
53. M. Dennis and I. Duling, "Experimental study of sideband generation in femtosecond fiber lasers," IEEE J. Quantum Electron. **30**(6), 1469–1477 (1994).
54. O. Kotlyar, M. Kamalian-Kopae, M. Pankratova, A. Vasylchenkova, J. E. Prilepsky, and S. K. Turitsyn, "Convolutional long short-term memory neural network equalizer for nonlinear Fourier transform-based optical transmission systems," Opt. Express **29**(7), 11254–11267 (2021).
55. S. Deligiannidis, A. Bogris, C. Mesaritakis, and Y. Kopsinis, "Compensation of fiber nonlinearities in digital coherent systems leveraging long short-term memory neural networks," J. Lightwave Technol. **38**(21), 5991–5999 (2020).
56. https://doi.org/10.15129/44de22fe-e9c5-455b-a5c2-40156914873a.
57. J. Hult, "A fourth-order Runge–Kutta in the interaction picture method for simulating supercontinuum generation in optical fibers," J. Lightwave Technol. **25**(12), 3770–3775 (2007).
58. A. M. Heidt, "Efficient adaptive step size method for the simulation of supercontinuum generation in optical fibers," J. Lightwave Technol. **27**(18), 3984–3991 (2009).
59. J. S. Feehan and J. H. V. Price, "Decoherence due to XPM-assisted Raman amplification for polarization or wavelength offset pulses in all-normal dispersion supercontinuum generation," J. Opt. Soc. Am. B **37**(3), 635–644 (2020).
60. J. S. Feehan, E. Brunetti, S. Yoffe, W. Li, S. M. Wiggins, D. A. Jaroszynski, and J. H. V. Price, "Noise-related polarization dynamics for femto and picosecond pulses in normal dispersion fibers," Opt. Express **28**(15), 21447–21463 (2020).
61. Corning, https://www.corning.com/media/worldwide/coc/documents/Fiber/SMF-28%20Ultra.pdf (2014). Accessed: 06/09/2021.
62. Y. Shen, G. Gao, Y. Meng, X. Fu, and M. Gong, "Gain-phase modulation in chirped-pulse amplification," Phys. Rev. A **96**(4), 043851 (2017).
63. R. L. Fork, C. H. B. Cruz, P. C. Becker, and C. V. Shank, "Compression of optical pulses to six femtoseconds by using cubic phase compensation," Opt. Lett. **12**(7), 483–485 (1987).
64. R. Casini and P. G. Nelson, "On the intensity distribution function of blazed reflective diffraction gratings," J. Opt. Soc. Am. A **31**(10), 2179–2184 (2014).
65. J. A. Nelder and R. Mead, "A simplex method for function minimization," The Computer Journal **7**(4), 308–313 (1965).

Optics EXPRESS

66. I. B. Gonzalo, R. D. Engelsholm, M. P. Sørensen, and O. Bang, "Polarization noise places severe constraints on coherence of all-normal dispersion femtosecond supercontinuum generation," Sci. Rep. **8**(1), 6579 (2018).
67. M. Brehler, M. Schirwon, D. Göddeke, and P. M. Krummrich, "A GPU-accelerated fourth-order Runge–Kutta in the interaction picture method for the simulation of nonlinear signal propagation in multimode fibers," J. Lightwave Technol. **35**(17), 3622–3628 (2017).